Tunable porous nanoallotropes prepared by post-assembly etching of binary nanoparticle superlattices

Tunable Porous Nanoallotropes Prepared from Binary Nanoparticle Superlattices Self-Assembled at the Liquid-Air Interface

Thumu Udayabhaskararao,[1] Thomas Altantzis,[2] Lothar Houben,[3,4] Marc Coronado-Puchau,[5] Judith Langer,[5] Ronit Popovitz-Biro,[3] Luis M. Liz-Marzán,[5,6,7] Lela Vuković,[8] Petr Král,[9,10,11] Sara Bals,[2] Rafal Klajn[1]*

[1]Department of Organic Chemistry, Weizmann Institute of Science, Rehovot 76100, Israel

[2]EMAT, University of Antwerp, Groenenborgerlaan 171, B-2020 Antwerp, Belgium

[3]Department of Chemical Research Support, Weizmann Institute of Science, Rehovot 76100, Israel

[4]Ernst Ruska-Centre for Microscopy and Spectroscopy with Electrons, 52425 Jülich, Germany

[5]CIC biomaGUNE, Paseo de Miramón 182, 20014 Donostia-San Sebastián, Spain

[6]Ikerbasque, Basque Foundation for Science, 48013 Bilbao, Spain

[7]Biomedical Research Networking Center in Bioengineering, Biomaterials, and Nanomedicine (CIBER-BBN), 20014 Donostia-San Sebastián, Spain

[8]Department of Chemistry, University of Texas at El Paso, El Paso, TX 79968, USA

[9]Department of Chemistry, University of Illinois at Chicago, Chicago, IL 60607, USA

[10]Department of Physics, University of Illinois at Chicago, Chicago, IL 60607, USA

[11]Department of Biopharmaceutical Sciences, University of Illinois at Chicago, Chicago, IL 60607, USA

*Correspondence to: rafal.klajn@weizmann.ac.il

Abstract: Self-assembly of inorganic nanoparticles has been used to prepare hundreds of different colloidal crystals, but almost invariably with the restriction that the particles must be packed densely. Here, we show that non-close-packed nanoparticle arrays can be fabricated by selective removal of one of two components comprising binary nanoparticle superlattices. First, a variety of binary nanoparticle superlattices were prepared at the liquid-air interface, including several arrangements that were previously unknown. Molecular dynamics simulations revealed the unique role of the liquid in templating the formation of superlattices not achievable by self-assembly in bulk solution. Second, upon stabilization, all of these binary superlattices could be transformed into distinct "nanoallotropes" – nanoporous materials having the same chemical composition, but differing in their nanoscale architectures.

One Sentence Summary: Binary nanoparticle arrays treated with etchants, selective for one of their components, are transformed into a new family of nanoporous materials.

Main Text: Self-assembly has emerged as the strategy of choice toward generating ordered arrays of nanosized particles. The resulting materials, in particular those assembled from inorganic nanoparticles (NPs) (*1-7*), often exhibit unanticipated optical (*8*), thermoelectric (*9*),

magnetic (*10*), catalytic (*11*), and other (*12*) properties. The diversity of structures and presumably the properties of these materials could be greatly increased via post-synthetic modifications. In particular, it would be of great interest to generate assemblies in which the constituent NPs are ordered yet separated by relatively large distances (i.e., non-close-packed nanoparticle arrays). Although several examples of related materials have been reported, they are limited to highly specific systems, such as those involving highly directional interactions (*13, 14*) or a fine balance between attractive and repulsive forces during self-assembly (*15*), and a general route to non-close-packed NP arrays has been lacking.

One strategy to tackle this limitation could be based on the selective removal (by means of chemical etching) of one type of NPs from binary nanoparticle superlattices (BNSLs) (*1*). Depending on the stoichiometry and structure of the initial BNSLs, this method could lead to "nanoallotropes" – materials having the same chemical composition, but differing in their nanoscale architecture. Unfortunately, within BNSLs, the two types of nanoscopic components mutually support each other, and removal of one would inevitably lead to the disruption of the other. Here, we hypothesized that this undesired behavior could be overcome by stabilizing the BNSL by controlled removal of the surfactants from the NP surfaces (*16-18*). If successful, this procedure would serve three purposes: *i*) attaching the NPs to the underlying surface, *ii*) controlling the coalescence of the NPs, and *iii*) activating the sacrificial component of the BNSL toward etching.

Our strategy is illustrated in Fig. 1A. We worked with monodisperse batches of Au and Fe_3O_4 NPs (Fig. S1, S2 in the Supplementary Materials), which we assembled at the diethylene glycol (DEG)-air interface (step 1 in Fig. 1A), as previously reported (*19*). Following transfer onto a carbon-coated transmission electron microscopy (TEM) copper grid (step 2) and a controlled, thermally induced desorption of ligands from the NPs (*17*) (step 3), the samples were exposed to an etchant reacting with only one of the two materials (step 4). For proof-of-concept, we co-assembled a ~1:1 mixture of 5.2 (±0.4) nm dodecanethiol-protected Au NPs and 10.6 (±0.6) nm oleate-protected Fe_3O_4 NPs into the previously reported (*19*) AB-type binary NP monolayer (Fig. 1B, center, Fig. S3-S5). Following immobilization onto carbon-coated TEM grids, Fe_3O_4 NPs could be etched out by immersing the substrate into an aqueous solution of HCl, without affecting the order of the gold NPs. Figure 1C, for example, shows an ensemble of 250 gold NPs, the positions of which all remained unaffected after HCl etching (see also Figs. S6-S8). We will refer to the resulting non-close-packed array of Au NPs as vac_1Au_1, where *vac* denotes "vacancy". Alternatively, a square array of Fe_3O_4 NPs could be obtained by treating the BNSLs with a cyanide solution, which can selectively dissolve Au NPs (Fig. 1B, right).

Importantly, the underlying substrate had a profound effect on the successful fixation of the NPs. The particles could be readily immobilized on commercial carbon-coated Formvar films as well as on homemade carbon-coated nitrocellulose substrates. However, we found no attachment onto silicon wafers or nitrocellulose lacking a layer of amorphous carbon (Fig. S9). From these experiments, we conclude that amorphous carbon facilitates the desorption of organic

ligands from the NP surfaces and the formation of a carbonaceous film (*20*), which can serve as an adhesive for the NPs. The carbonaceous films can directly be visualized by TEM, as shown in Fig. S10. Overall, the above procedure allows for the fabrication of non-close-packed NP superlattices on thin, flexible substrates (see the inset of Fig. 1B, left), which can subsequently be transferred onto surfaces of choice.

Self-assembly from a ~5:1 mixture of Au and Fe_3O_4 NPs resulted in a different type of BNSL, as shown in Fig. 2A (see also Fig. S11). This array, featuring alternating clusters of Au NPs and individual Fe_3O_4 NPs, is akin to the previously reported Fe_4C-type BNSL (*21*). However, selective removal of the Fe_3O_4 counterpart allowed us to clearly observe quintets—rather than quartets—of Au NPs arranged in a tetrahedral geometry (Figs. 2B, S12). To decipher the structure of this and other more complex assemblies (vide infra), we conducted electron tomography studies (*22*, *23*) by acquiring series of 2D projections of the etched arrays over a wide range of tilt angles using high-angle annular dark-field scanning transmission electron microscopy (HAADF-STEM). These studies confirmed that each cluster was composed of five Au NPs (giving rise to stoichiometry vac_1Au_5; see also Figs. S13-S15), and they helped elucidate the mutual packing of the resulting tetrahedra (Fig. 2C, D; see Section 5 of the Supplementary Materials for tomography data). The high stability of these tetrahedra could be attributed to partial coalescence of Au NPs, which occurs as a result of ligand desorption (*16*-*18*). As the structural model in Fig. S16 shows, the vac_1Au_5 array is derived from an incomplete (deficient in Au) AB_6-type BNSL.

An important feature of our method is that it allows us to control the degree of coalescence by adjusting the time of thermal treatment. This is illustrated in Fig. S17, where extending the heating time from 30 minutes to 6 hours enabled us to convert an ensemble of tetrahedra into a well-defined array of pseudospherical ~9 nm gold NPs (see also Figs. S18, S19). Interestingly, we identified another, unexpected effect of heating, where Au NP quintets lacking a strong attachment to the underlying substrate could migrate and be transformed into well-defined sinuous nanowires (Fig. S20).

Increasing the Au:Fe_3O_4 NP ratio to ~10 led to another type of BNSL, which, following the removal of Fe_3O_4, exhibited features (Figs. 2E, F, and S21-S23) reminiscent of the previously reported (*24*) AB_{13}-type BNSL. The AB_{13}-type BNSL is composed of layers of quartets and quintets of the "B" NPs, following a $(\text{-}B_4\text{-}B_5\text{-}B_4\text{-})_n$ pattern. However, electron tomography studies on our etched material revealed that it consisted of alternating layers of NP quartets and septets (i.e., a $(\text{-}B_4\text{-}B_7\text{-})_n$ pattern; Fig. 2G, H), corresponding to an AB_{11} stoichiometry of the precursor BNSL (see also the discussion in Fig. S24). Similar to the AB_6-type BNSLs, the AB_{11} arrays could be thermally transformed by partial sintering of the constituent Au NPs, resulting in nanoporous membranes (Fig. S25, *bottom*).

When, on the other hand, the ratio of Au to Fe_3O_4 NPs was decreased to ~4 and a more polydisperse batch of Au NPs (4.9 ± 0.7 nm) was used, we observed the formation of BNSLs, within which the Au NPs were arranged into zigzag-like patterns (Fig. S26). Electron tomography analysis showed that this BNSL consisted of stacked NP layers having an AB_4 stoichiometry

(Fig. 2I, J; Figs. S27 and S28), where "A" denotes a Fe_3O_4 NP and "B" – large, medium, and small Au NPs in a 1:2:1 ratio (for example, the non-close-packed array shown in Fig. 2I consists of 6.2 nm, 5.3 nm, and 4.1 nm Au NPs). The fact that highly crystalline arrays could be assembled even from relatively polydisperse batches of NPs highlights the tendency of NPs to maximize the packing at the DEG-air interface. In fact, analysis of the AB_4, AB_6, and AB_{11} BNSLs showed that they all share the same densely packed initial (bottom) monolayer (see Fig. 2D, H, J and the structural models in Figs. S16, S25, and S29).

The formation of the above AB_4, AB_6, AB_{11}, and other (see below) structures not observed during self-assembly in 3D (i.e., bulk solution) suggests a profound effect of DEG on the assembly process (*25, 26*). To disclose the mechanisms governing self-assembly in our system, we performed precise atomistic molecular dynamics (MD) simulations of NPs at different liquid-air interfaces. These simulations, detailed in Section 3 of the Supplementary Materials, revealed that the unique role of DEG in guiding NP self-assembly is due to a combination of several effects. First, the coupling energies of both types of NPs to DEG are large compared with the NP-NP coupling energies between exposed or partly submerged NPs (Tables S1, S2). Hence, the NPs exhibit a high affinity to the surface of the underlying liquid, which they tend to cover in the most efficient way. Second, both dodecanethiol-protected Au NPs and oleate-protected Fe_3O_4 NPs preferentially submerge in DEG to about half their diameter (Fig. 2K, L). As a result, DEG can organize the bottom layer of NPs in a way that may not be achievable during self-assembly in bulk solution. Finally, we found that the coupling energy of the NPs to DEG per unit surface area of NP is approximately the same for both types of NPs. Consequently, both Au and Fe_3O_4 NPs have a similar affinity towards the surface of DEG, from which they can displace each other during the self-assembly process. Taken together, these effects show that DEG can modify the free energies of BNSLs, favoring the formation of otherwise unstable BNSLs.

When the same polydisperse (4.9 ± 0.7 nm) Au and monodisperse 10.6 nm Fe_3O_4 NPs were used in a ~5:1 ratio, we observed the formation of an unprecedented quasi-ternary BNSL with a stoichiometry ABC_4, where "B" denotes a small (~4.0 nm) and "C" – a large (~5.5 nm) Au NP (Fig. S30). Subjecting this superlattice to our stabilization–etching procedure afforded a non-close-packed $vac_1Au_1Au'_4$ array shown in Fig. 2M-P (here, Au and Au′ denote small and large Au NPs, respectively) (see also Figs. S31-S34). We note that within the ABC_4-type BNSL, the bottom-most Au and Fe_3O_4 NPs have their bottom boundaries (rather than the equatorial cross-sections) at the same level. However, the "half-submergence condition" is still satisfied for both NP types if one considers the two 5.5 nm Au NPs placed on top of each other (labeled C and C′ in Fig. 2P) as a single, elongated NP. In fact, electron tomography studies could not resolve individual NPs within these putative dimers, suggesting that they undergo a partial coalescence (see cyan and red in Fig. 2O).

Importantly, our methodology could be extended to multilayers (Figs. S35-S44), which is exemplified for a novel AB_4-type BNSL (Figs. 3A, S40). This BNSL was obtained by co-assembly of

5.2 nm Au and 10.6 nm Fe_3O_4 NPs pre-mixed in a ~4:1 ratio, where the thickness of the superlattice depended on the amount of NPs applied at the liquid-air interface. For example, HAADF-STEM tomography revealed that the non-close-packed superlattice shown in Fig. 3B obtained by etching the corresponding BNSL (Fig. 3A) was a hexalayer (cf. Figs. 3C, S43; see also Section 5 of the Supplementary Materials). Upon extended (>1 hr) heating at 70 °C, the original AB_4-type array was transformed into the exotic pattern shown in Fig. 3D (see also Fig. S42), whose structure remains to be identified.

Our methodology can also be applied to NP building blocks of other sizes. This is first exemplified in Fig. 3F, G, where we extended the average distance between 5.2 nm Au NPs within vac_1Au_1 arrays from 12.5 to 15.3 nm by simply increasing the size of the Fe_3O_4 NPs with which they were co-assembled from 10.6 to 13.0 nm. These results indicate the ability to pattern solid substrates comprising nanoscopic Au domains, with sub-nanometer precision. When the sizes of both Au (5.2 nm) and Fe_3O_4 (10.6 nm) NPs were decreased (to 3.0 and 8.4 nm, respectively), many of the BNSLs and the resulting non-close-packed arrays could be recreated on a smaller scale (see Fig. S45). Similarly, working with mixtures of 5.2 nm Au NPs and 8.4 nm Fe_3O_4, we obtained AB-, AB_4-, ABC_4-type, and other BNSLs described above (Fig. S46). In addition, the modified NP size ratio resulted in novel NP arrays, such as the vac_1Au_2-type and the vac_4Au_2-type structures shown in Fig. 3H, I (see also Fig. S47).

We envision that non-close-packed nanoparticle arrays will have a wide range of interesting optical, mechanical, catalytic, and other properties. To this end, we examined several different NP arrays as substrates for surface-enhanced Raman scattering (SERS) and found that the vac_1Au_{11}-type array has superior signal enhancement properties (Fig. S51), which is in agreement with a significantly higher density of electromagnetic hotspots at gaps between NPs within the multilayer structure, into which analyte molecules can readily diffuse through the open crystalline lattice. We are currently testing the utility of our loosely packed NP arrays (e.g., Fig. 3G) as seeds / catalysts for the vertical growth of single-crystalline nanowires (*27*). An attractive avenue will be to utilize the well-defined nanopores within these materials for trapping protein molecules or even to reconstitute multienzyme complexes. An important aspect of our procedure is that it leads to surfactant-free gold surfaces, amenable to facile functionalization with thiolated ligands. Our results on multilayers suggest that this method could be readily extended to three-dimensional assemblies, including binary superlattices comprising non-spherical NPs (*28*), quasicrystalline arrays (*29*), and ternary superlattices (*30*). In the future, the diversity of the nanostructured materials will be further expanded by performing additional post-synthetic transformations (such as ion exchange and galvanic replacement reactions) on binary nanoparticle superlattices.

References and Notes:

1. E. V. Shevchenko, D. V. Talapin, N. A. Kotov, S. O'Brien, C. B. Murray, Structural diversity in binary nanoparticle superlattices, *Nature* **439**, 55-59 (2006).

2. N. A. Kotov, F. C. Meldrum, C. Wu, J. H. Fendler, Monoparticulate Layer and Langmuir-Blodgett-Type Multiparticulate Layers of Size-Quantized Cadium-Sulfide Clusters - A Colloid-Chemical Approach to Superlattice Construction, *J. Phys. Chem.* **98**, 2735-2738 (1994).
3. S. Y. Park, A. K. R. Lytton-Jean, B. Lee, S. Weigand, G. C. Schatz, C. A. Mirkin, DNA-programmable nanoparticle crystallization, *Nature* **451**, 553-556 (2008).
4. Z. Y. Tang, Z. L. Zhang, Y. Wang, S. C. Glotzer, N. A. Kotov, Self-assembly of CdTe nanocrystals into free-floating sheets, *Science* **314**, 274-278 (2006).
5. D. Nykypanchuk, M. M. Maye, D. van der Lelie, O. Gang, DNA-guided crystallization of colloidal nanoparticles, *Nature* **451**, 549-552 (2008).
6. G. Singh, H. Chan, A. Baskin, E. Gelman, N. Repnin, P. Král, R. Klajn, Self-assembly of magnetite nanocubes into helical superstructures, *Science* **345**, 1149-1153 (2014).
7. T. Wang, J. Q. Zhuang, J. Lynch, O. Chen, Z. L. Wang, X. R. Wang, D. LaMontagne, H. M. Wu, Z. W. Wang, Y. C. Cao, Self-Assembled Colloidal Superparticles from Nanorods, *Science* **338**, 358-363 (2012).
8. E. V. Shevchenko, M. Ringler, A. Schwemer, D. V. Talapin, T. A. Klar, A. L. Rogach, J. Feldmann, A. P. Alivisatos, Self-assembled binary superlattices of CdSe and Au nanocrystals and their fluorescence properties, *J. Am. Chem. Soc.* **130**, 3274-3275 (2008).
9. M. Ibanez, Z. S. Luo, A. Genc, L. Piveteau, S. Ortega, D. Cadavid, O. Dobrozhan, Y. Liu, M. Nachtegaal, M. Zebarjadi, J. Arbiol, M. V. Kovalenko, A. Cabot, High-performance thermoelectric nanocomposites from nanocrystal building blocks, *Nat. Commun.* **7**, 10766 (2016).
10. A. G. Dong, J. Chen, X. C. Ye, J. M. Kikkawa, C. B. Murray, Enhanced Thermal Stability and Magnetic Properties in NaCl-Type FePt-MnO Binary Nanocrystal Superlattices, *J. Am. Chem. Soc.* **133**, 13296-13299 (2011).
11. Y. J. Kang, X. C. Ye, J. Chen, Y. Cai, R. E. Diaz, R. R. Adzic, E. A. Stach, C. B. Murray, Design of Pt-Pd Binary Superlattices Exploiting Shape Effects and Synergistic Effects for Oxygen Reduction Reactions, *J. Am. Chem. Soc.* **135**, 42-45 (2013).
12. J. J. Urban, D. V. Talapin, E. V. Shevchenko, C. R. Kagan, C. B. Murray, Synergism in binary nanocrystal superlattices leads to enhanced p-type conductivity in self-assembled PbTe/Ag_2Te thin films, *Nat. Mater.* **6**, 115-121 (2007).
13. M. P. Boneschanscher, W. H. Evers, J. J. Geuchies, T. Altantzis, B. Goris, F. T. Rabouw, S. A. P. van Rossum, H. S. J. van der Zant, L. D. A. Siebbeles, G. Van Tendeloo, I. Swart, J. Hilhorst, A. V. Petukhov, S. Bals, D. Vanmaekelbergh, Long-range orientation and atomic attachment of nanocrystals in 2D honeycomb superlattices, *Science* **344**, 1377-1380 (2014).
14. H. X. Lin, S. M. Lee, L. Sun, M. Spellings, M. Engel, S. C. Glotzer, C. A. Mirkin, Clathrate colloidal crystals, *Science* **355**, 931-935 (2017).
15. A. M. Kalsin, M. Fialkowski, M. Paszewski, S. K. Smoukov, K. J. M. Bishop, B. A. Grzybowski, Electrostatic self-assembly of binary nanoparticle crystals with a diamond-like lattice, *Science* **312**, 420-424 (2006).

16. C. J. Kiely, J. Fink, M. Brust, D. Bethell, D. J. Schiffrin, Spontaneous ordering of bimodal ensembles of nanoscopic gold clusters, *Nature* **396**, 444-446 (1998).
17. Y. X. Yu, C. A. Bosoy, D. M. Smilgies, B. A. Korgel, Self-Assembly and Thermal Stability of Binary Superlattices of Gold and Silicon Nanocrystals, *J. Phys. Chem. Lett.* **4**, 3677-3682 (2013).
18. T. Altantzis, Z. J. Yang, S. Bals, G. Van Tendeloo, M. P. Pileni, Thermal Stability of $CoAu_{13}$ Binary Nanoparticle Superlattices under the Electron Beam, *Chem. Mater.* **28**, 716-719 (2016).
19. A. G. Dong, J. Chen, P. M. Vora, J. M. Kikkawa, C. B. Murray, Binary nanocrystal superlattice membranes self-assembled at the liquid-air interface, *Nature* **466**, 474-477 (2010).
20. Y. C. Jiao, D. D. Han, Y. Ding, X. F. Zhang, G. N. Guo, J. H. Hu, D. Yang, A. G. Dong, Fabrication of three-dimensionally interconnected nanoparticle superlattices and their lithium-ion storage properties, *Nat. Commun.* **6**, 6420 (2015).
21. E. V. Shevchenko, D. V. Talapin, C. B. Murray, S. O'Brien, Structural characterization of self-assembled multifunctional binary nanoparticle superlattices, *J. Am. Chem. Soc.* **128**, 3620-3637 (2006).
22. H. Friedrich, C. J. Gommes, K. Overgaag, J. D. Meeldijk, W. H. Evers, B. de Nijs, M. P. Boneschanscher, P. E. de Jongh, A. J. Verkleij, K. P. de Jong, A. van Blaaderen, D. Vanmaekelbergh, Quantitative Structural Analysis of Binary Nanocrystal Superlattices by Electron Tomography, *Nano Lett.* **9**, 2719-2724 (2009).
23. M. P. Boneschanscher, W. H. Evers, W. K. Qi, J. D. Meeldijk, M. Dijkstra, D. Vanmaekelbergh, Electron Tomography Resolves a Novel Crystal Structure in a Binary Nanocrystal Superlattice, *Nano Lett.* **13**, 1312-1316 (2013).
24. E. V. Shevchenko, D. V. Talapin, S. O'Brien, C. B. Murray, Polymorphism in AB_{13} nanoparticle superlattices: An example of semiconductor-metal metamaterials, *J. Am. Chem. Soc.* **127**, 8741-8747 (2005).
25. V. Aleksandrovic, D. Greshnykh, I. Randjelovic, A. Fromsdorf, A. Kornowski, S. V. Roth, C. Klinke, H. Weller, Preparation and electrical properties of cobalt-platinum nanoparticle monolayers deposited by the Langmuir-Blodgett technique, *ACS Nano* **2**, 1123-1130 (2008).
26. A. G. Dong, X. C. Ye, J. Chen, C. B. Murray, Two-Dimensional Binary and Ternary Nanocrystal Superlattices: The Case of Monolayers and Bilayers, *Nano Lett.* **11**, 1804-1809 (2011).
27. X. D. Wang, C. J. Summers, Z. L. Wang, Large-scale hexagonal-patterned growth of aligned ZnO nanorods for nano-optoelectronics and nanosensor arrays, *Nano Lett.* **4**, 423-426 (2004).
28. X. C. Ye, J. Chen, M. Engel, J. A. Millan, W. B. Li, L. Qi, G. Z. Xing, J. E. Collins, C. R. Kagan, J. Li, S. C. Glotzer, C. B. Murray, Competition of shape and interaction patchiness for self-assembling nanoplates, *Nat. Chem.* **5**, 466-473 (2013).
29. Z. J. Yang, J. J. Wei, P. Bonville, M. P. Pileni, Beyond Entropy: Magnetic Forces Induce Formation of Quasicrystalline Structure in Binary Nanocrystal Superlattices, *J. Am. Chem. Soc.* **137**, 4487-4493 (2015).
30. W. H. Evers, H. Friedrich, L. Filion, M. Dijkstra, D. Vanmaekelbergh, Observation of a Ternary Nanocrystal Superlattice and Its Structural Characterization by Electron Tomography, *Angew. Chem. Int. Ed.* **48**, 9655-9657 (2009).

Acknowledgments: This work was supported by the European Research Council (grants 336080 CONFINEDCHEM to R.K. and 335078 COLOURATOM to S.B.), the Rothschild Caesarea Foundation (R.K.), the NSF (Division of Materials Research, grant #1506886) (P.K.), and the startup funding from the University of Texas at El Paso (L.V.). L.M.L.-M. acknowledges funding from the Spanish Ministerio de Economía y Competitividad (grant MAT2013-46101-R). T.A. acknowledges funding from the Research Foundation Flanders (FWO, Belgium) through a postdoctoral grant. The computer support was provided by the Texas Advanced Computing Center.

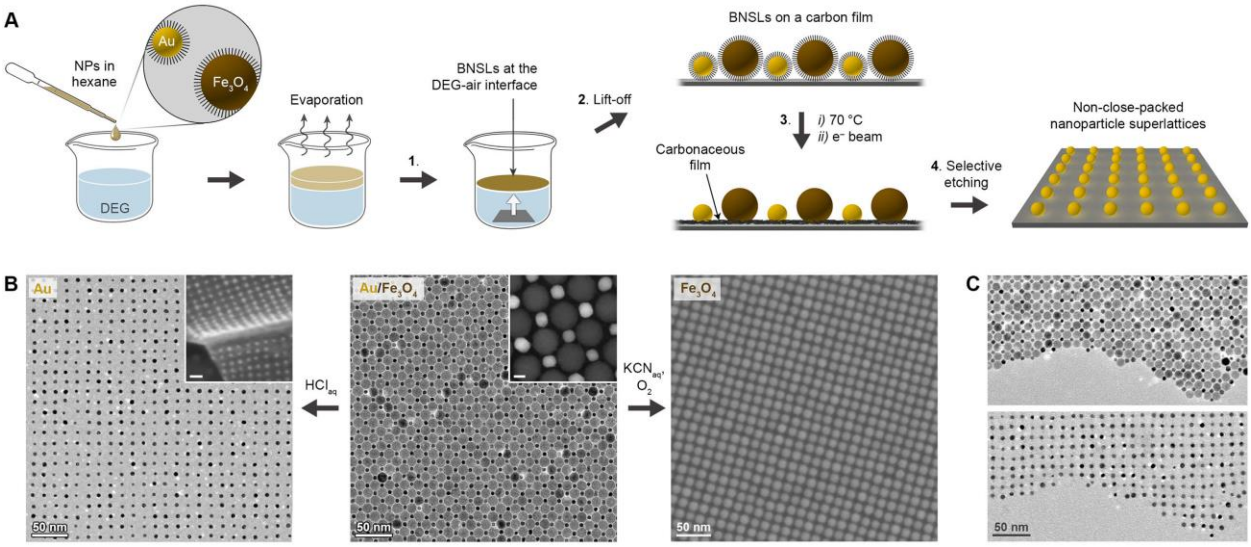

Fig. 1. Preparation of non-close-packed nanoparticle arrays. (**A**) Schematic illustration of the method ("e^- beam" denotes a ~10 min exposure to the electron beam of a transmission electron microscope (TEM); NPs = nanoparticles; BNSL = binary nanoparticle superlattice). (**B**) *Center:* TEM image of an AB-type BNSL. The image in the inset was recorded in HAADF-STEM mode. *Left:* TEM image of a non-close-packed array of Au NPs (vac_1Au_1) obtained by selective removal of Fe_3O_4. Inset: scanning electron microscopy (SEM) image showing the flexible nature of the underlying film. *Right:* SEM image of a non-close-packed array of Fe_3O_4 NPs obtained by selective removal of Au. Scale bars in the insets correspond to 5 nm (center) and 20 nm (left). (**C**) An edge of an AB-type BNSL before (top) and after (bottom) Fe_3O_4 etching.

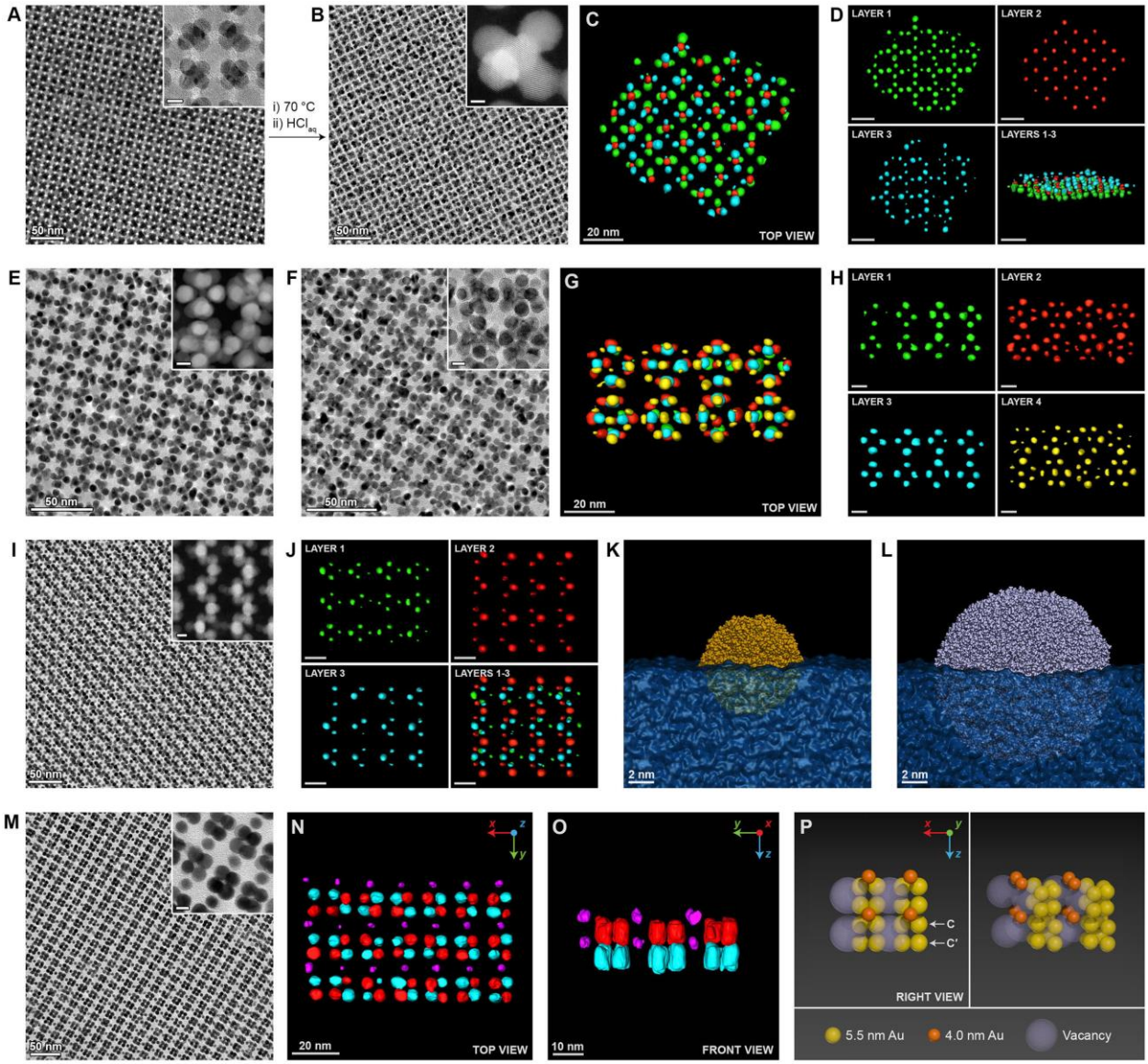

Fig. 2. Structural diversity and characterization of non-close-packed nanoparticle arrays. (**A**) TEM image of an AB_6-type BNSL (here, lacking the top layer of Au NPs). (**B**) TEM image of a vac_1Au_5-type array. (**C**) 3D representation of a part of the reconstructed segmented volume of a vac_1Au_5-type array. The different colors correspond to different layers of NPs along the *z*-axis. (**D**) Different layers of the vac_1Au_5 array shown separately for clarity. In the bottom right image, the structure is tilted by 80-85° around the *x*-axis. The scale bars correspond to 20 nm. (**E, F**) TEM images of vac_1Au_{11}-type arrays terminated with two different layers of Au NPs. (**G**) 3D representation of a part of the reconstructed segmented volume of a vac_1Au_{11}-type array at different viewing directions. (**H**) Four different layers of a vac_1Au_{11}-type array shown separately for clarity. Scale bars = 10 nm. (**I**) TEM image of a $vac_1Au_1Au_2'Au''_1$-type array (Au, Au′, and Au″ denote differently sized Au NPs). (**J**) Four different layers of a $vac_1Au_1Au_2'Au''_1$-type array shown separately for clarity. Scale bars = 20 nm. (**K, L**) Atomistic models of a dodecanethiol-functionalized 5 nm Au NP (K) and an oleate-functionalized 10 nm Fe_3O_4 NP (L) relaxed at the

DEG-vacuum interface. (**M**) TEM image of a $vac_1Au_1Au'_4$-type array. (**N**, **O**) 3D representation of a part of the reconstructed segmented volume of a $vac_1Au_1Au'_4$-type array at different viewing directions. In (O), entities colored in red and cyan correspond to two Au NPs on top of each other. (**P**) Structural model of the $vac_1Au_1Au'_4$-type array. The images in the insets in B, E, and I have been recorded in an HAADF-STEM mode. Scale bars in the insets correspond to 5 nm.

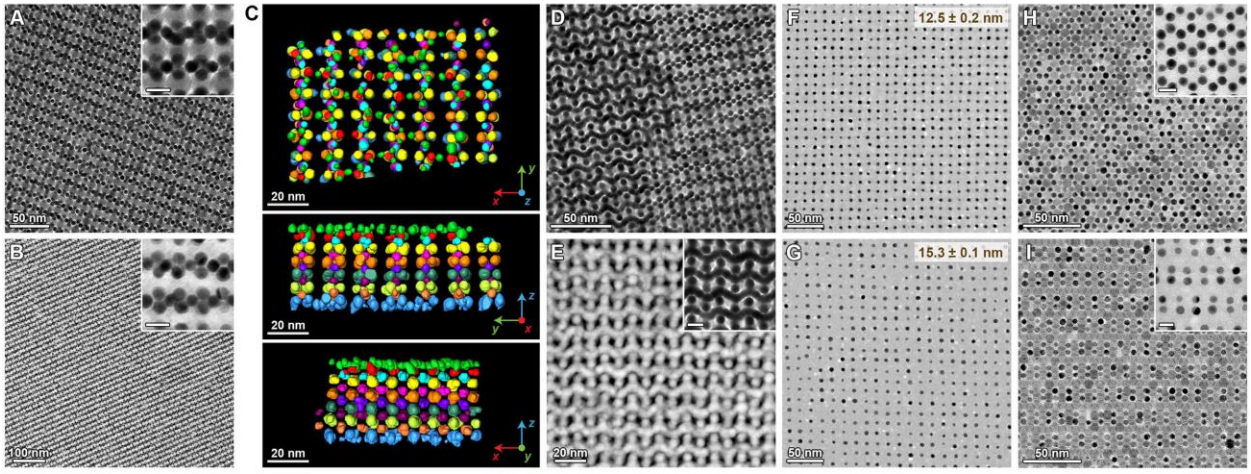

Fig. 3. Extension to multilayers and other nanoparticle sizes. (A) TEM image of an AB_4-type binary superlattice. (**B**) TEM image of a vac_1Au_4-type array. (**C**) 3D representation of a part of the reconstructed segmented volume of a hexalayer of a vac_1Au_4-type array at different viewing directions. (**D**) TEM image showing the coexistence of two different types of AB_4 BNSLs and the epitaxial relationship between them. (**E**) HAADF-STEM image of a vac_1Au_4-type array. (**F**, **G**) TEM images of vac_1Au_1-type arrays obtained from BNSLs co-assembled from 5.2 nm Au NPs with (F) 10.6 nm and (G) 13.0 nm Fe_3O_4. (**H**) TEM image of an AB_2-type BNSL and the corresponding (post-etching) vac_1Au_2-type array (inset). (**I**) TEM image of an A_2B-type BNSL and the corresponding vac_2Au-type array (inset). Scale bars in the insets correspond to 10 nm.

Supplementary Materials:

Materials and Methods

Figures S1-S51

Tables S1-S3

Tomography data

References (*31-52*)